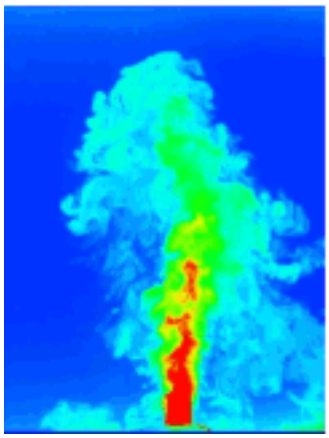

Journal of Turbulence
Publication details, including instructions for authors and subscription information:
http://www.tandfonline.com/loi/tjot20

Pressure fluctuation in high-Reynolds-number turbulent boundary layer: results from experiments and DNS

Yoshiyuki Tsuji [a], Shintaro Imayama [b], Philipp Schlatter [b], P. Henrik Alfredsson [b], Arne V. Johansson [b], Ivan Marusic [c], Nicholas Hutchins [c] & Jason Monty [c]

[a] Department of Energy Engineering and Science, Nagoya University, Chikusa-ku, Furo-cho, Japan

[b] Linné FLOW Center, KTH Mechanics, Stockholm, Sweden

[c] Department of Mechanical Engineering, The University of Melbourne, Parkville, Victoria, Australia

Version of record first published: 08 Nov 2012.

To cite this article: Yoshiyuki Tsuji, Shintaro Imayama, Philipp Schlatter, P. Henrik Alfredsson, Arne V. Johansson, Ivan Marusic, Nicholas Hutchins & Jason Monty (2012): Pressure fluctuation in high-Reynolds-number turbulent boundary layer: results from experiments and DNS, Journal of Turbulence, 13, N50

To link to this article: http://dx.doi.org/10.1080/14685248.2012.734625

Journal of Turbulence
Vol. 13, No. 50, 2012, 1–19

Pressure fluctuation in high-Reynolds-number turbulent boundary layer: results from experiments and DNS

Yoshiyuki Tsuji[a]*, Shintaro Imayama[b], Philipp Schlatter[b], P. Henrik Alfredsson[b], Arne V. Johansson[b], Ivan Marusic[c], Nicholas Hutchins[c], and Jason Monty[c]

[a]*Department of Energy Engineering and Science, Nagoya University, Chikusa-ku, Furo-cho, Japan*
[b]*Linné FLOW Center, KTH Mechanics, Stockholm, Sweden*
[c]*Department of Mechanical Engineering, The University of Melbourne, Parkville, Victoria, Australia*

(*Received 15 December 2011; final version received 11 September 2012*)

We have developed a small pressure probe and measured both static pressure and wall pressure simultaneously in turbulent boundary layers up to Reynolds numbers based on the momentum thickness $R_\theta \simeq 44{,}620$. The measurements were performed at large experimental facilities in Sweden, Australia, and Japan. We find that the measured pressure data are contaminated by the artificial background noise induced by test section and are also affected by the flow boundary conditions. By analyzing data from different wind tunnels acquired at the same Reynolds number, we evaluate the effect of background noises and boundary conditions on the pressure statistics. We also compare the experimental results with results of direct numerical simulations and discuss differences in boundary conditions between real and simulated wind tunnels.

Keywords: turbulent boundary layer; static-pressure fluctuation; outer and inner scaling; wall pressure; background noise; flow boundary conditions; direct numerical simulation

1. Introduction

Several years ago, in the first experiment to focus on the pressure statistics in high-Reynolds-number turbulence, we measured the instantaneous pressure fluctuations in the turbulent boundary layer [1]. The results were reported in TSFP4 [2] and TSFP5 [3]. These studies showed that pressure fluctuations measured inside the boundary layer are affected by the free-stream condition. Wall-pressure fluctuations have a certain correlation with static pressure even at twice the boundary layer thickness, while the corresponding velocity fluctuation correlation is negligible.

We expect a potential flow to exist in the free stream outside the boundary layer. The turbulent intensity, however, is not zero and is maintained as small as possible in the experiments. The free-stream-intensity ratio ($u_{\rm rms}/U_0$, here U_0 is the free-stream mean velocity and $u_{\rm rms}$ is the root mean square of streamwise velocity fluctuation) is arranged to be smaller than 0.1 %, which is a fundamental requirement for turbulent boundary layer experiments. However, the intensity of pressure fluctuations has yet to be studied in detail. It is not zero outside the boundary layer, which is associated with the fact that $u_{\rm rms}$ itself has a nonzero value.

*Corresponding author. Email: c42406a@nucc.cc.nagoya-u.ac.jp

ISSN: 1468-5248 online only

http://dx.doi.org/10.1080/14685248.2012.734625
http://www.tandfonline.com

In a wind tunnel, an inherent contamination of the pressure signal results from artificial noises related to the wind tunnel fan and, for example, possible separation zones in the return circuit. These acoustic disturbances are of low frequency (generally well below 100 Hz). From the Navier–Stokes equation, we obtain the Poisson equation for the instantaneous pressure $\widetilde{p}$ [4]. The pressure is thus calculated based on the source terms and boundary conditions. If acoustic disturbances are contained in the source term, then the question arises as to whether this effect can be removed to evaluate the physical pressure inside the boundary layer.

The flow boundary conditions also affect the pressure statistics. Boundary conditions vary depending on the type of wind tunnel. Typical wind tunnels are either a closed-circular type or a blowing type. Inflow and outflow conditions vary between these types. Another important factor for the boundary conditions is the manner in which the flat plate inside the test section is set up. In the Stockholm wind tunnel, the plate is arranged at the middle of the test section so that the flow blows along both sides of the plate. In the Kyushu and Melbourne tunnels, the boundary layer develops over the bottom wall of test section. In the case of the numerical wind tunnel, the flow boundary conditions differ slightly among the numerical codes adopted for the calculation. They are also different from those of experimental wind tunnels. The question of how these different boundary conditions affect the pressure statistics is addressed herein.

Experimental data were obtained by the same person using the same techniques at the large facilities in Stockholm (Sweden), Melbourne (Australia), and Kyushu (Japan). In this paper, we compare these data with the pressure statistics from relatively high-Re-number direct numerical simulation (DNS) by Schlatter and Örlü [5] and by Jiménez et al. [6]. The numerical wind tunnel does not introduce artificial noise. Then, such a comparison should show how to treat the effect of artificial noise in experimental data. As the experimental data are measured by the same technique at different facilities, data comparison teaches us how boundary conditions affect the pressure statistics. It is interesting to note that the boundary conditions in DNS might be different from the experimental boundary conditions. If the boundary conditions for the Poisson equation vary depending on the facilities (or on the simulation code used), can we expect universality of pressure statistics inside the boundary layer? These are the main concerns in the present study, and the data for high-Re-number flow data should be useful in addressing these issues.

2. Experimental conditions

Pressure fluctuations in the flow field are measured with a standard static-pressure tube probe (Figure 1). Calibration techniques allow us to remove the part of the signal related

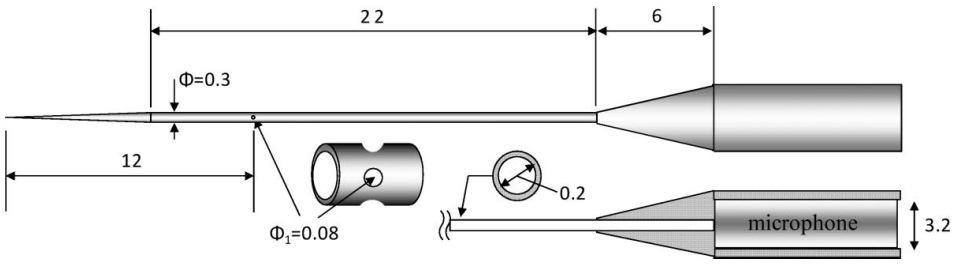

Figure 1. Schematic view of pressure probe.

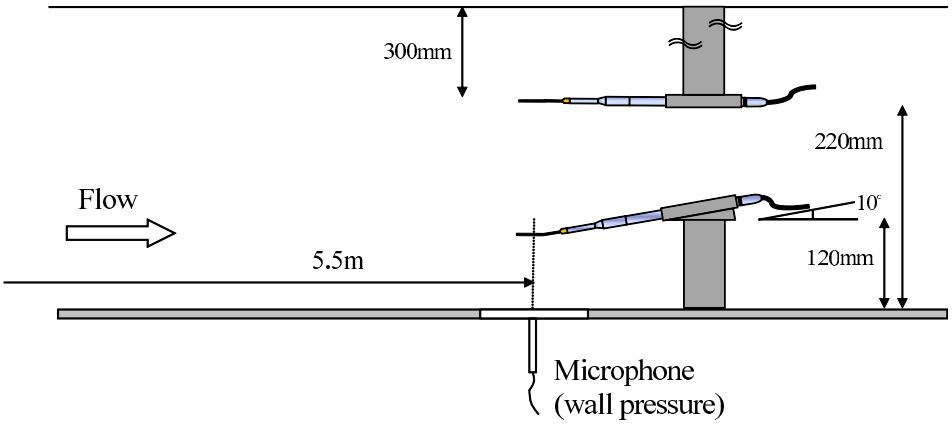

Figure 2. Configuration of probes in the test section of the Stockholm wind tunnel.

to Helmholtz resonance and the standing waves generated in the tube [1]. The probe body consists of two stainless steel tubes joined by threaded and screwed junctions; the windward tube is cone shaped and equipped with four static pinholes spaced 90° apart in the circumferential direction and located 12 mm from the tip. This tube has pinhole diameters of $\phi_1 = 0.12$ mm, an inner diameter of $\phi = 0.5$ mm, and a tube material thickness of $h = 0.05$ mm. Another smaller one has the dimension of $\phi_1 = 0.08$ mm, $\phi = 0.3$ mm, and $h = 0.05$ mm. The leeward tube begins with a standard 1/8-inch condenser microphone with a diameter $d_M = 3.2$ mm. In a previous measurement [1], we used a probe with 0.6 mm outer diameter and $\phi_1 = 0.15$ mm, which was attached to the 1/4-inch microphone. Therefore, the present probe is approximately half the size of the previous one. The microphone allows measurements in the frequency range of $10 \sim 70 \times 10^3$ Hz, where the lower-frequency limit is restricted by its mechanical system. The dynamic range is $2 \times 10^{-2} \sim 3.2 \times 10^3$ Pa, which means that relatively small amplitudes can be measured.

A schematic view of probe setting in the wind tunnel is shown in Figure 2. Here, a specially designed wall-normal traversing system is used that protrudes from the plate and allows us to traverse in the range $0 \leq y \leq 2\delta$, where δ is the boundary layer thickness. Another reference probe is positioned in the free stream, 30 cm from the upper wall surface, and measures pressure fluctuations outside the boundary layer. In the present context, we refer to a static-pressure fluctuation simply as a pressure fluctuation and denote it as $\widetilde{p_s}$. The pressure fluctuation outside the boundary layer measured by the reference probe is denoted as $\widetilde{p_r}$ and is called the reference pressure or the free-stream pressure.

The 1/4-inch microphone is mounted in the cavity volume behind the surface, which is arranged to be as small as possible. The pinhole diameter is $d = 0.3$ mm and its depth is $\ell = 1.0$ mm. Hence, the aspect ratio is $\ell/d = 3.33$. From the discussion in [1], the error is estimated to be minimal. The wall-pressure fluctuation is denoted by $\widetilde{p_w}$. Wall pressure, static pressure inside the boundary layer, and background pressure in the free stream are measured simultaneously. The reference pressure is used to remove the artificial background noise generated in the wind tunnel (such as acoustic, instrument, and vibration noises) . The experiments were performed in the KTH (Kungliga Tekniska Högskolan) wind tunnel in Sweden [7], in the Melbourne wind tunnel in Australia [8, 9], and in the Kyushu wind tunnel in Japan [10]. The characteristics of the flow field are summarized in Table 1. The

Table 1. Characteristics of the flow field in the wind tunnel facilities used for the present measurement; L is the measurement location distance from the leading edge, R_θ is the Reynolds number based on momentum thickness θ and the free-stream velocity U_0, δ is the boundary layer thickness taken at $U(\delta) = 0.99U_0$, and u_τ is friction velocity.

Facility	L (m)	δ (cm)	θ (cm)	R_θ	U_0 (m/s)	u_τ (m/s)
Sweden	5.5	$5.3 \sim 6.3$	$0.78 \sim 1.03$	$5870 \sim 18{,}300$	$8.3 \sim 34.0$	$0.33 \sim 1.14$
Australia	8, 13, 21	$13.8 \sim 33.8$	$13.6 \sim 26.9$	$8970 \sim 44{,}620$	$10 \sim 25$	$0.35 \sim 0.80$
Japan	10.95	$18.0 \sim 21.6$	$1.8 \sim 2.5$	$8200 \sim 28{,}300$	$5 \sim 25$	$0.17 \sim 0.79$

Reynolds number was varied up to $R_\theta \simeq 44{,}620$. Streamwise velocity is measured by a standard single hot wire, and the wall shear stress is obtained by oil film interferometry. The free-stream intensities are maintained in the range $0.02\% \sim 0.04\%$.

The sources of the DNS data used for comparison are listed in Table 2. The detailed numerical conditions are given in the original papers. Through careful procedures, these simulations calculate the zero-pressure-gradient boundary layers, although they differ in the flow domain size, tripping type, and initial flow conditions, etc., and are different among them. These parameters might affect the numerical results, as reported by Schlatter and Örlü [5], who noted that the shape factor, skin friction coefficient, and root mean square (rms) of the streamwise velocity component differ considerably between the various DNS databases. In the wind tunnel experiments, such discrepancies have also been observed [14] and are caused by different configurations of the various facilities, different sensors, and different experimental techniques. Although these discrepancies are usually discussed in terms of velocity statistics, we will discuss this problem herein from the viewpoint of pressure statistics.

3. Results and discussions

3.1. *Background noise*

Instantaneous pressure fluctuations at the wall, inside the boundary layer, and in the free stream are expressed as $\widetilde{p_w}$, $\widetilde{p_s}$, and $\widetilde{p_r}$, respectively. These pressures are decomposed into their mean and fluctuation as

$$\begin{aligned} \widetilde{p_w} &= P_w + p_w, \\ \widetilde{p_s} &= P_s + p_s, \\ \widetilde{p_r} &= P_r + p_r. \end{aligned} \tag{1}$$

Table 2. DNS compared with experimental data. Detailed numerical conditions are referred to original studies.

Authors	R_θ	Numerical method	Transition
Spalart [11]	300, 600, 1410	Spectral	Periodic domain
Skote [12]	383–716	Spectral	Tripping
Jiménez et al. [6]	1000, 1550, 1968	Finite difference/spectral	Rescaling, recycling
Schlatter and Örlü [5]	677–4271	Spectral	Tripping
Wu and Moin [13]	400–800	Finite difference	Free-stream disturbances

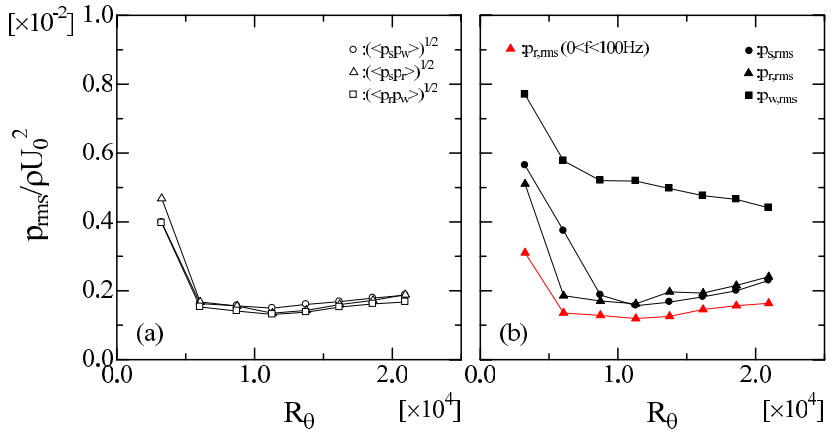

Figure 3. Correlations between p_w, p_s, and p_r measured at the Stockholm wind tunnel. A static-pressure probe is positioned at $y = 120$ mm from the wall, which is twice the boundary layer thickness.

A preliminary measurement has been performed in the Stockholm wind tunnel. The static-pressure probe is fixed at $y = 120$ mm, which is about twice the boundary layer thickness. The pressure fluctuations $\widetilde{p_w}$, $\widetilde{p_s}$, and $\widetilde{p_r}$ are measured simultaneously. The correlations among p_w, p_s, and p_r, which are expressed as $\langle p_s p_w \rangle$, $\langle p_s p_r \rangle$, and $\langle p_w p_r \rangle$, are normalized by outer variables and are plotted against Reynolds number in Figure 3(a). In this case, the correlation $\langle p_s p_r \rangle$ is associated with the flow at the outer edge of the boundary layer as the static-pressure probe is set at $y = 120$ mm ($\simeq 2\delta$) and the reference probe is at $y = 220$ mm as shown in Figure 2. The correlation $\langle p_w p_r \rangle$ between the wall and the reference pressure represents the large-scale fluctuations across the test section. These values are almost constant as a function of Reynolds number when they are normalized by outer variables and are similar in intensity, that is, $\langle p_s p_r \rangle \simeq \langle p_w p_r \rangle \simeq \langle p_s p_w \rangle$. This result means that large-scale pressure fluctuations exist across the boundary layer and they are commonly contained in p_w, p_s, and p_r. In Figure 3(b), the root mean squares of p_w, p_s, and p_r are plotted against the Reynolds number. These quantities are expressed as $p_{w,\mathrm{rms}}$, $p_{s,\mathrm{rms}}$, and $p_{r,\mathrm{rms}}$, respectively. The results show that the wall pressure is twice as large as the reference pressure, but the reference pressure seems to be relatively large. As discussed below, the artificial background noise that contaminates p_s and p_w must be removed using the knowledge of p_r. After such a correction, the background pressure becomes much smaller than the wall pressure. Similar effects of contamination are observed at the wind tunnels in Australia and Japan, although the manner in which p_r and p_s are contaminated differs for these wind tunnels. A detailed comparison of the results from three facilities will be summarized in a future presentation.

In a regular measurement, the static-pressure probe is scanned across the boundary layer from $y/\delta = 0.024$ to $y/\delta = 1.53$. The premultiplied cross spectra of p_s and p_w are plotted in Figure 4, in which the frequency is multiplied, and are expressed as the premultiplied spectrum (PMS), specifically,

$$\mathrm{PMS} = f \times E_{sw}(f),$$
$$\langle p_s p_w \rangle = \int_0^{+\infty} \mathrm{PMS} d\ln f = \int_0^{+\infty} E_{sw}(f) df \,. \tag{2}$$

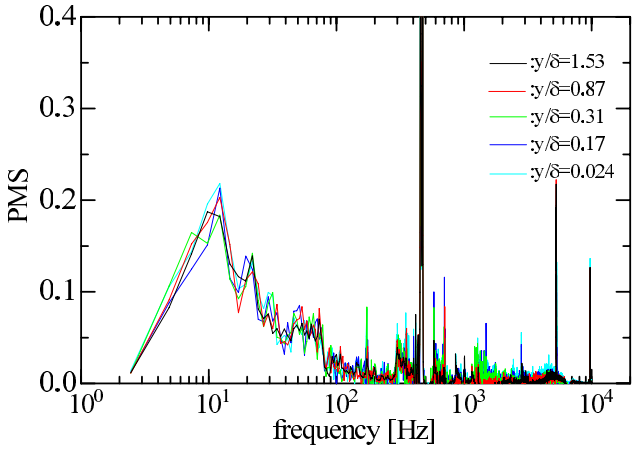

Figure 4. Premultiplied spectra of cross correlation between p_w and p_s. Position of the static-pressure probe varies from $y/\delta = 0.024$ to $y/\delta = 1.53$ at $R_\theta = 11{,}260$.

The sharp spike around 450 Hz corresponds to the frequency of the wind tunnel fan. We find that the PMS shows a similar distribution independent of y/δ, and that the dominant contribution to the spectrum comes from the low-frequency region ($f \leq 100$ Hz). So the free-stream pressure fluctuations span a wide area of the boundary layer. This is consistent with the result that the correlation $\langle p_r p_w \rangle$ is approximately equal to $\langle p_r p_s \rangle$ as indicated in Figure 3(a). We are interested in the correlations caused by the nonlocal feature of pressure and herein address the question of whether the correlation $\langle p_r p_w \rangle$ is associated with physical phenomena in the boundary layer or with artificial noise in the facilities. We compute the intensity of reference pressure, whose contribution is limited in the region of $f < 100$ Hz, and show the result in Figure 3(b) (red triangles). Compared with the original background intensities (black triangles), we observe that the free-stream signal consists mostly of large-scale fluctuations.

From this analysis, we assume that free-stream pressure fluctuations penetrate into the boundary layer all the way to the wall. Conversely, close to the wall are large pressure variations generated by strong turbulence, which also influence the pressure outside the boundary layer. Therefore, the wall pressure has a nonnegligible correlation with the pressure at the edge of the boundary layer. This is significantly different from the velocity correlation. Thus, from the results shown in Figure 4, we conclude that the static pressure inside the boundary layer is contaminated by the free-stream pressure. In the wind tunnel, the artificial background noise (expressed as p_b hereafter) adds to the physical pressure fluctuations. Background noise is generated by acoustic disturbances, wind tunnel fan noise, vibration noise, etc. In order to remove the background effect, we usually set up the reference probe at the appropriate position and correct the measured pressure by means of its signal. Therefore, we suggest the following decomposition by the assumption that the background pressure is represented by the reference pressure.

$$\begin{aligned} p_s &= p_s' + p_b \simeq p_s' + p_r, \\ p_w &= p_w' + p_b \simeq p_w' + p_r, \end{aligned} \tag{3}$$

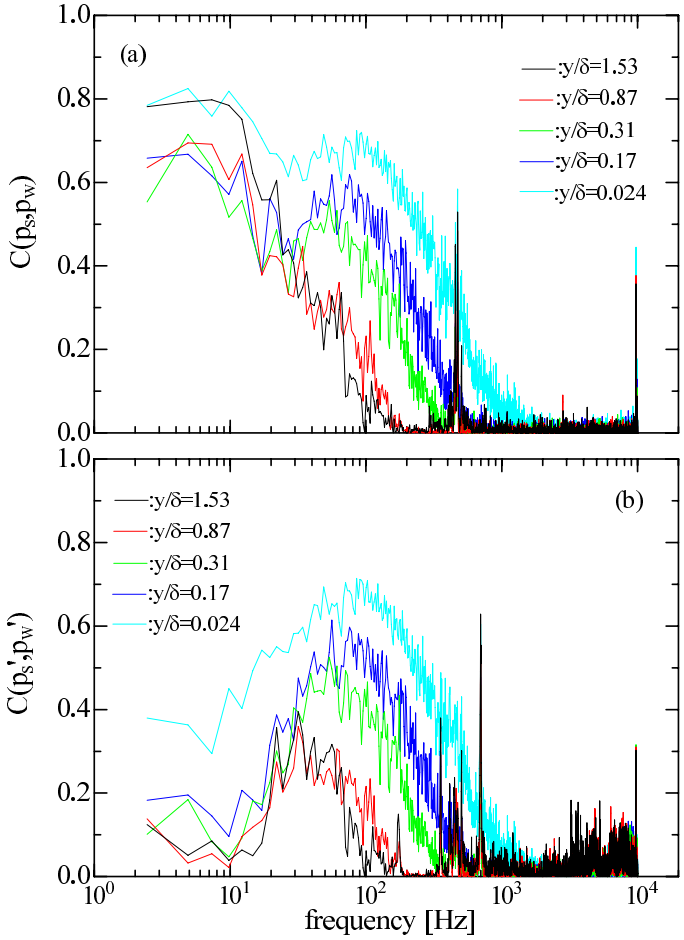

Figure 5. Correlation-coefficient spectra defined by Equation (4). Static-pressure probe position varies from $y = 0$ mm to $y = 120$ mm at $R_\theta = 11{,}260$: (a) original signal, (b) background pressure is subtracted.

where p'_s and p'_w are static- and wall-pressure fluctuations other than the background pressure. In Figure 5(a), we plot the correlation-coefficient spectra for p_s and p_w, as defined by Equations (4) and (6), at several points in the boundary layer. The quantity $C(p_s, p_w)$ is large in the low-frequency region ($f \leq 100$ Hz), which is consistent with the trend observed in Figure 4. In addition, $C(p_s, p_w)$ is large and close to the wall region. If the instantaneous background pressure is subtracted, the correlation between wall pressure and static pressure inside the boundary layer is expressed as the correlation between p'_s and p'_w. This correlation is given by the coefficient $C(p'_s, p'_w)$ and is plotted in Figure 5(b).

$$C(p_s, p_w) = [E_{p_s p_w}]^2/[E_{p_s p_s} E_{p_w p_w}],$$
$$C(p'_s, p'_w) = [E_{p'_s p'_w}]^2/[E_{p'_s p'_s} E_{p'_w p'_w}], \quad (4)$$

where we define the following averages:

$$\begin{aligned}
\langle p_s p_w \rangle &= \int_0^{+\infty} E_{p_s p_w}(f)df, \quad \langle p'_s p'_w \rangle = \int_0^{+\infty} E_{p'_s p'_w}(f)df, \\
\langle p_s^2 \rangle &= \int_0^{+\infty} E_{p_s p_s}(f)df, \quad \langle p_s'^2 \rangle = \int_0^{+\infty} E_{p'_s p'_s}(f)df, \\
\langle p_w^2 \rangle &= \int_0^{+\infty} E_{p_w p_w}(f)df, \quad \langle p_w'^2 \rangle = \int_0^{+\infty} E_{p'_w p'_w}(f)df \, .
\end{aligned} \tag{5}$$

The correlation-coefficient spectrum $C(p'_s, p'_w)$ differs significantly from $C(p_s, p_w)$ in the low-frequency region, since the background pressure is subtracted in the former case. However, even when the background pressure is subtracted, the static pressure p'_s at $y/\delta = 1.53$ exhibits some positive correlation with wall pressure p'_w.

3.2. *Correction of background pressure*

We decompose the measured pressure into physical pressure and background pressure through Equations (2) and (3). This calculation is based on the assumption that the physical pressure is independent of background pressure and that the background pressure is represented by the reference pressure measured in the free stream. The correction of the background pressure effect has been tested by several researchers, but these earlier attempts have been for surface-wall-pressure measurement. Measurements of wall-pressure fluctuation are complicated since the propagating acoustic pressure fluctuations generated by the flow facilities are superimposed on the pressure fluctuations produced by turbulence. Furthermore, the pressure sensor signal is also contaminated by vibrations of the wall to which the sensor is attached. Agarwal and Simpson tried to remove the wall vibration using three sensors [15]. Lauchle and Daniels [16] modified the classical noise cancelation technique to include vibration-induced effects on the pressure transducer signal. However, this latter technique can be used only for axisymmetric acoustic modes of pipe flow. Simpson et al. [17] and McGrath and Simpson [18] proposed a technique to cancel the acoustic noise contributions to the microphone signal in a wind tunnel with two-dimensional mean flow. In contrast to the conventional-, subtraction-based, noise-cancelation methods, Naguib et al. [19] developed an optimal-filter scheme, which is particularly useful for conditions of low signal-to-noise ratio and therefore is well suited for low-to-moderate Reynolds number measurements. In addition, their scheme is not limited to extracting the turbulent statistics but can be used to obtain the noise-canceled time series.

From Equations (2) and (3), p'_s can be expressed as $p'_s = p_s - p_r$. The root mean squares of these values are written as $p'_{s,\mathrm{rms}}$, $p_{s,\mathrm{rms}}$, and $p_{r,\mathrm{rms}}$, respectively. The pressure p'_s is expected to be a static pressure inside the boundary layer in which the background effect is not present. Comparing $p'_{s,\mathrm{rms}}$ with the pressure obtained by DNS, we find that $p'_{s,\mathrm{rms}}$ is slightly larger than the value obtained by DNS, which may be because the background pressure is not sufficiently removed, or because the present reference pressure p_r cannot accurately represent the background effect. Artificial noises generated by wind fans, acoustic noise, standing waves in the tunnel, etc., are all contained in p_b. However, we assume that these sources of noise are not completely represented by p_r. We measure the reference pressure at one point in the free stream, but the probe array should be set up in the wind

tunnel to monitor the background effect. In wind-tunnel experiments, the pressure inside the tunnel may affect the pressure at any point. The present analysis shows the difficulty in separating the artificial noises generated by the flow condition from the physical pressure fluctuations.

There is no artificial background noise in the numerical wind tunnel, but this condition cannot be achieved in a real wind tunnel. Thus, the measured pressure should always be larger than the result obtained by DNS. In order to compare the pressure profiles inside the boundary layer in experimental and numerical simulations, the artificial background pressure should be adequately corrected. In the present study, the static-pressure intensity is corrected by the following relation:

$$p''_{s,\mathrm{rms}} = p_{s,\mathrm{rms}} + C_1\sqrt{\langle p_r p_s\rangle} + C_2\,. \tag{6}$$

The constants C_1 and C_2 are determined by matching the outer normalized value $p''_{s,\mathrm{rms}}/(\rho U_0^2)$ with the value obtained by DNS in the free stream. This procedure is based on the assumption that the physical pressure intensity in the free stream is relatively small and is dominated by the artificial background noise. In Figure 8(a), we plot the normalized pressure intensities at $y = 2\delta$ from typical numerical simulations. The results of Schlatter and Örlü and Jiménez et al. show a similar trend. Skote's simulation gives a higher value whereas the data by Wu and Moin [13] give smaller values. Wu and Moin's simulation shows a decreasing trend against Reynolds number because the boundary layer is not fully developed. From the plot in Figure 8(a), we learn that the normalized pressure intensity is independent of the Reynolds number but that its value depends on the numerical simulation code used by each researcher. This point will be discussed further in Section 3.4. Here, we compare the experiment with DNS, and adjust the pressure intensity in the free stream to that of relatively high-Reynolds-number DNSs by Schlatter and Örlü [5] and Jiménez et al. [6]. The constants C_1 and C_2 are determined from Equation (6) and the normalized intensity satisfies the condition $p''_{s,\mathrm{rms}}/(\rho U_0^2) = 2 \times 10^{-4}$ at $y = 2\delta$. Both C_1 and C_2 are independent of Reynolds number but depend on the measurement location from the leading edge and on the wind tunnel. In the Stockholm wind tunnel (closed circuit), $C_1 = -0.15$ and $C_2 = -1.1$. In the Melbourne wind tunnel (nonclosed circuit, blowing), $C_1 = -0.08$, $C_2 = -1.61$ ($x = 21$ m), $C_1 = 0.04$, $C_2 = -1.61$ ($x = 13$ m), and $C_1 = 0.26$, $C_2 = -1.88$ ($x = 8$ m). These different values indicate that the background noise contaminates the physical pressure in a different manner.

3.3. *Static-pressure intensity inside the boundary layer*

When the rms of pressure is normalized by outer variables ρU_0^2 and the distance from the wall with Δ, the profiles more or less collapse on each other in the outer region, as shown in Figure 6. Here Δ is the Rotta–Clauser boundary layer thickness and U_0 is the free-stream velocity. In Figure 6(a), the present measurement is compared with our previous study at almost the same Reynolds number. When the background noises are corrected by Equation (6), the pressure intensities are plotted in Figure 6(b) with DNS results. Figure 6(c) shows the results of DNS by Skote [12], Spalart [11], and Schlatter and Örlü [5]. Near the wall, we recognize a Reynolds number dependence for small R_θ. As the Reynolds number increases, the peak $p_{\mathrm{rms,max}}/\rho U_0^2$ increases and moves closer to the wall in terms of y/Δ. In the outer region, the normalized values collapse fairly well for different Reynolds numbers. But the convergent values depend on the numerical simulations. For the DNS of Schlatter and Örlü,

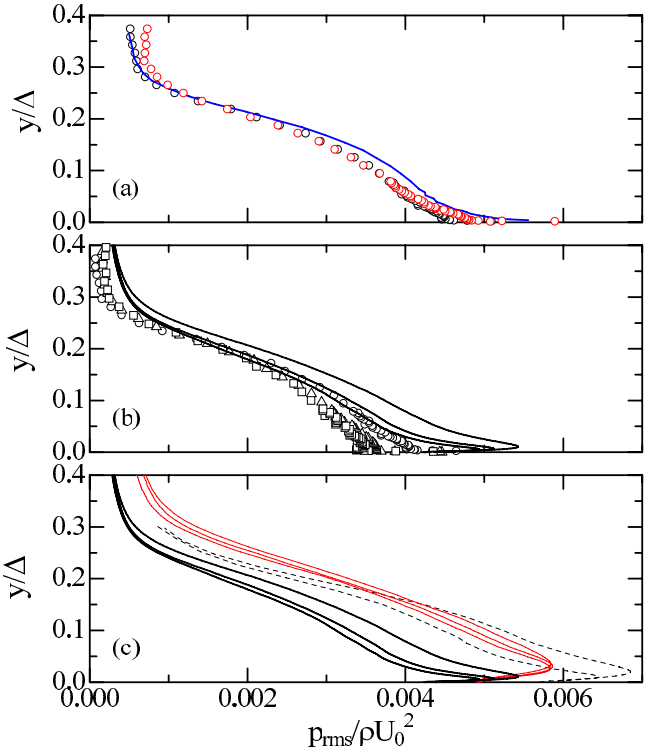

Figure 6. Pressure intensity measured at the Stockholm wind tunnel: (a) rms of the static pressure, normalized by twice the free-stream mean velocity and fluid density. ◯ (black): $R_\theta = 11{,}130$ measured by $(\phi, \phi_1) = (0.5\text{ mm}, 0.15\text{ mm})$ probe, ◯ (red): $R_\theta = 11{,}130$ measured by $(\phi, \phi_1) = (0.3\text{ mm}, 0.08\text{ mm})$ probe. Solid blue line is the result in our previous study at $R_\theta = 10{,}500$ [1]. (b) Pressure intensities are corrected according to Equation (6). ◯: $R_\theta = 11{,}130$, △: $R_\theta = 16{,}000$, □: $R_\theta = 20{,}700$. (c) Similar distributions obtained with DNS. Solid red lines are from Skote [12] at $R_\theta = 450, 716$, dashed lines are from Spalart [11] at $R_\theta = 670, 1410$, and solid lines are from Schlatter and Örlü [5] at $R_\theta = 2000, 3270, 4060$.

$p_{\rm rms}/\rho U_0^2$ at $y/\Delta = 0.4$ is 2.5×10^{-4} independent of Reynolds number. Skote's simulation gives a larger value, and Spalart's simulation gives a result between these two.

When the pressure intensity is normalized by inner variables, $p^+_{s,\rm rms} \equiv p''_{s,\rm rms}/(\rho u_\tau^2)$, a clear R_θ independence appears throughout the boundary layer [see Figure 7(a)]. The inner rms peak $p^+_{\rm rms,max}$ is around $y^+_p \simeq 30$ in the DNS but cannot be resolved experimentally due to the interaction of the physical probe with the wall. The probe used in this study cannot get closer to the wall than $y^+ \approx 100$ in the Stockholm wind tunnel. In the Melbourne and Kyushu wind tunnels, the boundary layer is thick relative to the probe size, thus allowing measurements closer to the wall. In the following, we only analyze the data except very close to the wall region. The probe resolution is an important issue but it is outside of the present study. This problem should be discussed in the next stage. DNSs show that the maximum value $p^+_{\rm rms,max}$ increases with Reynolds number. This Reynolds number dependence is shown by solid red symbols in Figure 7(b). The distributions are well approximated by a logarithmic function: $p^+_{\rm rms,max} \propto \ln(R_\theta)$. The same logarithmic relation is observed in the pressure at the location $y^+ = 100$. The DNS and experimental data are plotted by

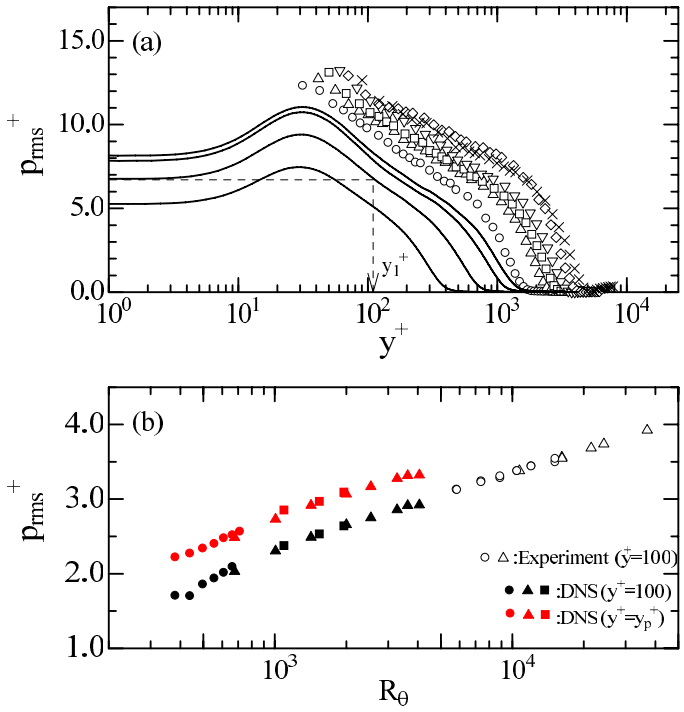

Figure 7. (a) Static-pressure intensities corrected according to Equation (6). Pressure is normalized by inner variables. ◯: $R_\theta = 5870$, △: $R_\theta = 7420$, □: $R_\theta = 8920$, ▽: $R_\theta = 10{,}500$, ◇: $R_\theta = 12{,}100$, ×: $R_\theta = 15{,}200$ at the Stockholm wind tunnel. Solid lines are DNS by Schlatter and Örlü [5]. (b) rms at $y^+ = 100$ with (◯) symbols at the Stockholm wind tunnel, and (△) symbols at the Melbourne wind tunnel versus the Reynolds number. Solid red symbols indicate the peak of $p^+_{\rm rms}$ obtained from DNS; ●: Skote [12], ■: Jiménez et al. [6], ▲: Schlatter and Örlü [5]. Solid black symbols are pressure intensities obtained by DNS at $y^+ = 100$.

solid and open symbols, respectively. Both data show a similar dependence on Reynolds number.

3.4. *Effect of boundary conditions on pressure statistics in numerical simulations*

Although the normalized pressure intensities at $y = 2\delta$ in Figure 8(a) are constant as a function of Reynolds number, the normalized pressure in the free-stream region, that is, at the outer edge of the computational domain, indicates a slightly different trend as plotted in Figure 8(b). The results for normalized pressure from Skote and Schlatter and Örlü are independent of Reynolds number, but those of Jiménez et al. and Wu and Moin increase with Reynolds number albeit at different levels. Wu and Moin's values are multiplied by 10^{-8}, thus $p_{\rm rms}$ is $O(10^{-10})$, which is very small compared with the other simulations. This result is due to the relatively large domain size in Wu and Moin's simulation (even though only discretized with few grid points). Simens et al. [20] pointed out that "the intensity of free-stream velocity fluctuations turns out to be controlled by the ratio between the height of the computational box and the boundary layer thickness at the exit". Therefore, from

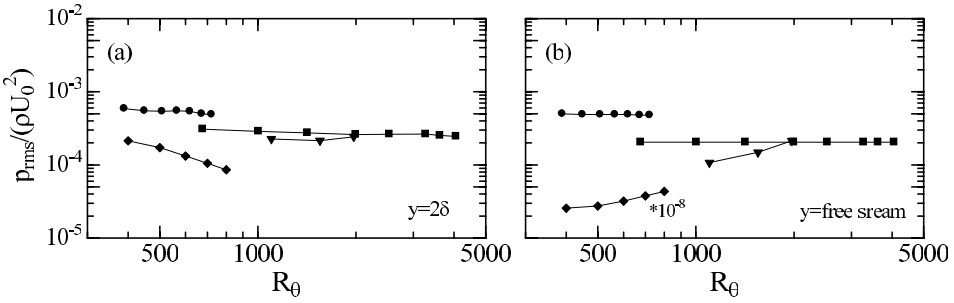

Figure 8. (a) Root mean square of static pressure at $y = 2\delta$ normalized by twice the free-stream mean velocity and fluid density. (b) Root mean square of static pressure at the free stream normalized by twice the free-stream mean velocity and fluid density. Data obtained from DNSs by ●: Skote [12], ■: Schlatter and Örlü [5], ▼: Jiménez et al. [6], ♦: Wu and Moin [13].

this example, we conclude that not only the velocity but also the pressure fluctuations are affected by domain size.

The upper-wall condition for a numerical wind tunnel may affect the computational results. For a top surface condition, Lund et al. [21] adopted $dU/dy = dW/dy = 0$, $V = U_0 d\delta_*/dy$, where δ_* is the displacement thickness. Lee and Sung used $U = U_0$, $dV/dy = dW/dy = 0$ [22], and Ferrante and Elghobashi [23] adopted the condition $U = 0, dV/dy = dW/dy = 0$, and $P = 0$. In real experiments, however, the flat plate is inserted inside the wind tunnel and the upper wall, located at a finite distance from the bottom plate, is adjustable. A narrow slit is arranged on the upper wall to balance the pressure inside the test section with atmospheric pressure. Thus, the upper-wall conditions are different from those used in DNSs.

The outflow from the test section is evaluated assuming the convective boundary conditions $\partial U/\partial t + U_c \partial U/\partial x = 0$, where U_c is usually the free-stream velocity at the exit [20, 22, 23]. For the simulations based on the Fourier decomposition in the streamwise direction, the periodic boundary conditions in the streamwise direction are combined with a spatially developing boundary layer by adding a "fringe region" at the end of the domain [24]. In this region, the outflow is forced via a volume force to a laminar inflowing velocity profile. The method allows the boundary layer growth normal to the wall to be rescaled, and thus, the physical domain and the fringe region together satisfy periodic boundary conditions. In a real wind tunnel, the outflow condition depends on the type of wind tunnel. If the tunnel discharges its flow to the atmosphere at the exit of the test section, it is called an open-circuit tunnel. Such a wind tunnel normally has a diffuser downstream of the test section. The kinetic energy of the air discharged from the diffuser is a small percentage of that of the air in the test section. A popular configuration for small tunnels is the blower type with the impeller at the entry. The Melbourne wind tunnel is a blowing-type open-circuit wind tunnel. In a closed-circuit wind tunnel, the same air is recirculated. The airstream is turned in four steps of nominally 90° each. There is always a small vent or breather somewhere in the circuit so that the internal pressure does not increase. In addition, because the air heats up during the run, a cooling system is indispensable. Such a tunnel usually has a slot around the perimeter at the downstream end of the test section so that the exit pressure is close to atmospheric pressure. This strategy reduces the effect of leaks through the holes cut in the walls. The Stockholm and Kyushu wind tunnels are of the

closed-circuit type. Thus, the outflow boundary condition depends on the wind tunnel type and may differ from the boundary conditions adopted in DNS.

The inflow conditions are summarized by Liu and Pletcher [25], who compared three methods for creating appropriate inflow conditions: the random fluctuation method [26], the matching database method [27], and the recycling method [11, 21]. They reported that the recycling method appears to establish a turbulent shear flow with a fairly short inlet buffer zone and provides accurate downstream profiles. The recycling method was introduced by Spalart and the concept was further developed by Lund et al. who introduced a rescaling idea. In their implementation, instantaneous profiles at a specific station are recycled to the inlet at each numerical step after rescaling. A method for generating inflow conditions for DNS of a spatially developing turbulent boundary layer is presented by Ferrante and Elghobashi [23] who modified the method of Lund et al. [21]. Keating et al. [28] found that the spectral content of the inflow velocity is important. Nikitin [29] has shown that a memory of the inflow condition persists in the spatially evolving flow for a considerable distance downstream of the inlet. The inflow effect is recently reported using DNS data by Schlatter and Örlü [30]. Any type of recycling will inevitably lead to temporal and spatial correlation in the velocity field. In the simulation by Skote [12] and Schlatter and Örlü [5], the inflow condition is laminar Blasius flow, which is perturbed to go through laminar-turbulent transition as in a wind tunnel.

As briefly summarized above, the boundary conditions may differ for the various numerical simulations. Such differences in boundary conditions and other numerical conditions have been focused on with regard to analyzing the velocity data. Schlatter and Örlü [5] pointed out that a DNS should be considered as a numerical experiment and that the results should be subjected to the same scrutiny as experimental data. We agree with their conclusion. A similar trend was observed in the pressure field, but no direct comparison has been made among numerical databases to date. Alfredsson and Örlü [31] suggested a simple test to evaluate the velocity data, in which a diagnostic plot is made as shown in Figure 9, where P_0 and P are the mean pressure in the free stream and inside the boundary layer at position y, respectively. Usually, in the boundary layer, the statistical quantities are plotted against distance from the wall, but it is a difficult task to measure the accurate distance from the wall. This plot is useful even if the exact y position is not known. In the graph, the upper-right part corresponds to the near-wall region ($y \to 0$), where the pressure intensity p_{rms} increases. The lower-left part shows the outer region of the boundary layer ($y \to +\infty$), where the pressure intensity is constant as indicated in Figure 6. In the outer region, we expect turbulence intensities to scale with outer variables and to be independent of Reynolds number. Skote's results indicate that p_{rms}/U_0^2 exhibits a reasonably good scaling. However, the results of Jiménez et al. do not collapse and their values increase with Reynolds number. Thus, the pressure they find at the edge of the boundary layer is not scaled by U_0. Near the wall region, Skote's results show that the ratio p_{rms}/U_0^2 does not collapse and depends on Reynolds number. Jiménez et al. [6] show, on the contrary, the overlapping of the data. From the diagnostic plot, we understand that the data from these two DNSs scale differently at the outer edge and near the wall, and that the numerical conditions, such as boundary conditions, initial flow, domain sizes, etc., remain in the calculated pressure field.

3.5. *Effect of boundary conditions on pressure statistics in experiments*

Figure 10 shows the intensity of pressure fluctuation normalized by outer length Δ and inner velocity scale u_τ. This kind of plot has been adopted in numerical research (see, e.g., [6,24]). With increasing Reynolds number, DNS results (solid lines) show that the peak

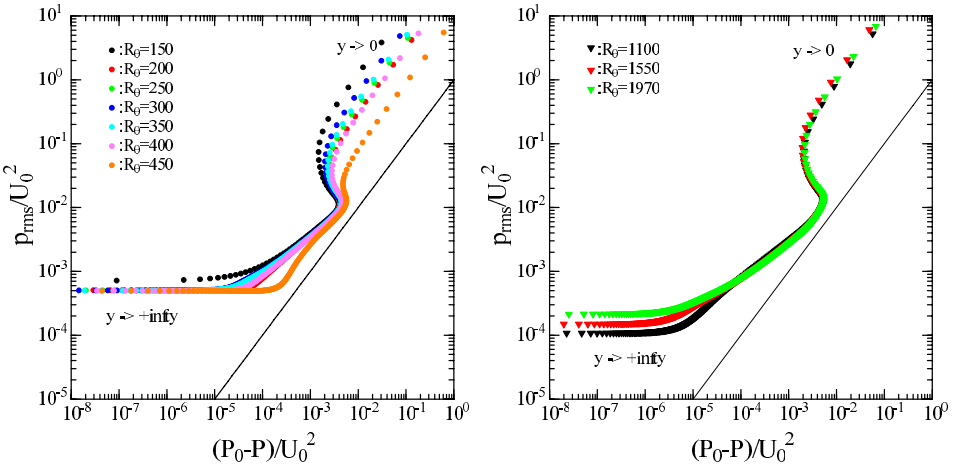

Figure 9. (a) Diagnostic plot of pressure intensity versus mean pressure from DNS data by Skote [12]. Pressure data are normalized by twice the free-stream mean velocity. (b) Diagnostic plot of pressure intensity versus mean pressure from DNS data by Jiménez et al. [6]. Pressure data are normalized by twice the free-stream mean velocity. Solid line indicates the relation: $p_{\rm rms} = P_0 - P$.

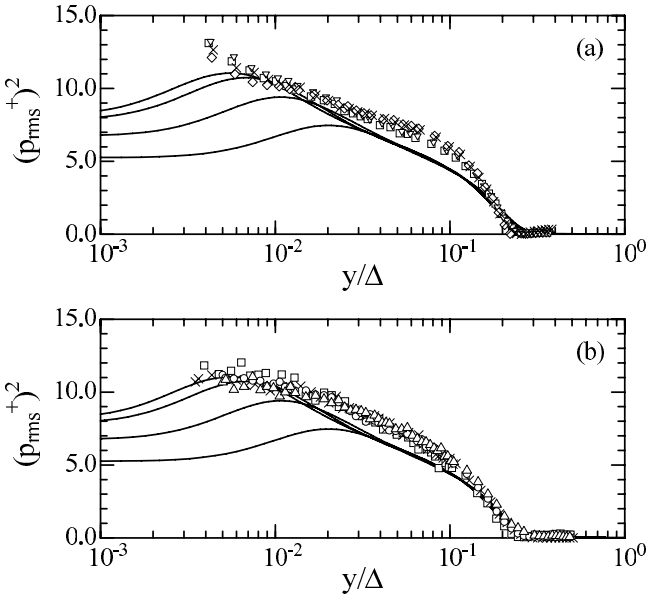

Figure 10. Root mean square of static pressure normalized using inner and outer variables: (a) pressure data measured in the Stockholm wind tunnel. □: $R_\theta = 8920$, ▽: $R_\theta = 10{,}500$, ◇: $R_\theta = 12{,}100$, ×: $R_\theta = 15{,}200$; (b) pressure data measured in the Melbourne wind tunnel. ◯: $R_\theta = 10{,}720$ ($x = 8$ m), △: $R_\theta = 16{,}180$ ($x = 8$ m), □: $R_\theta = 16{,}170$ ($x = 13$ m), ×: $R_\theta = 21{,}480$ ($x = 21$ m). Solid lines are DNS by Schlatter and Örlü [5] at $R_\theta = 1000, 2000, 3270, 4060$.

value increases and that its y-position approaches the wall. In the outer region, we find that the data overlap well and that the empirical relationship $(p^+_{\rm rms})^2 \propto \ln(y/\Delta)$ approximates the data. The experimental data are plotted on the same graph. Different symbols indicate the variation of Reynolds number. Figure 10(a) shows the results acquired in the Stockholm wind tunnel and Figure 10(b) shows the results obtained in the Melbourne wind tunnel. The similar Reynolds number range ($10{,}000 \leq R_\theta \leq 16{,}500$) in each facility is indicated. The background pressure is subtracted according to Equation (6). Although the experimental data appear to be sufficiently collapsed in the outer region of the boundary layer using the given scaling, they are slightly larger than the profiles obtained by DNS. The scaling is also confirmed and satisfied in larger Reynolds number ranges (up to $R_\theta \simeq 37{,}000$). Outside the boundary layer ($y/\delta > 1$), the normalized intensity is almost zero. By comparing the profiles measured in the two different facilities, we find first that the pressure intensity in the experiment is larger than that of DNS, and second, that the pressure in Stockholm is not the same as the values measured in Melbourne. This fact may be due to the background pressure not being perfectly removed from the physical pressure by means of Equation (6). Alternatively, the reference pressure p_r measured outside the boundary layer not only is the artificial noise but still contains the physical pressure associated with turbulence. The Stockholm wind tunnel is a closed-circuit type and the Melbourne wind tunnel is a blowing type. The upper-wall conditions are also different. If the background pressure depends on the flow boundary conditions such as inflow, outflow, and upper-wall flow, then the inside static pressure p_s also depends on these flow boundary conditions. As shown in Figure 5, the correlation $\langle p_s p_r \rangle$ remains nonzero inside the boundary layer. It may be difficult to completely remove the background effect from the measured pressure signal. Here we only adopt the pressure p_r measured at a single point outside the boundary layer. However, we need to refer to the pressure at several locations in the flow to correct for the background effect, and the pressure probe array may be an adequate setting for this purpose.

In the wind tunnel experiments, we cannot avoid the effect of boundary conditions on the pressure statistics and we need to adequately correct the background effect. Otherwise, the experimental values are always larger than the results of DNS. If the effects of boundary conditions and background noises are not correctly removed, we cannot expect universality of pressure statistics throughout the boundary layer.

3.6. *Wall-pressure intensity*

In the previous study, we have reported the dependence of wall-pressure rms on Reynolds number when pressure is normalized by inner, outer, and mixed scaling [1]. The wall pressure has also been corrected using Equation (6). The constants C_1 and C_2 are determined by the following procedure. From the results of DNS, we find that the static-pressure intensity inside the boundary layer $p_{s,\rm rms}$ equals the wall-pressure intensity $p_{w,\rm rms}$ at a given distance from the wall. This location is expressed as y_1^+, as shown in Figure 7, and seems to be constantly independent of Reynolds number. Analyzing the DNS data in detail, we find $y_1^+ \simeq 110$ when the Reynolds number is relatively large ($R_\theta > 2000$), as plotted in Figure 11. This empirical result is useful for determining the constants in Equation (6). From the static-pressure measurement at $y^+ = 110$, the intensity $p_{s,\rm rms}$ is matched to the wall-pressure intensity so as to determine the parameters C_1 and C_2. These constants are independent of Reynolds numbers but vary according to the wind tunnel or the locations where the sensors are mounted within the test section. For the Stockholm wind tunnel, we find $C_1 = -0.15$, $C_2 = -0.3$, while for the Melbourne wind

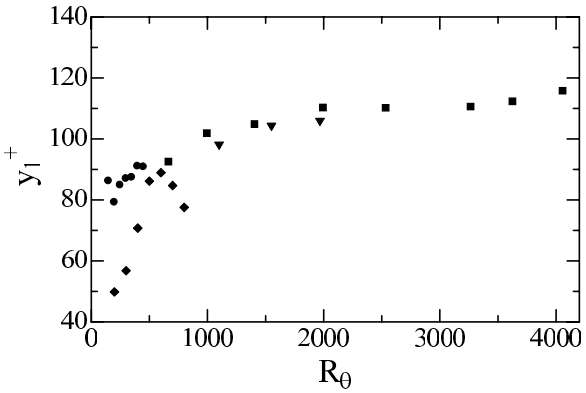

Figure 11. y_1^+ is distance from the wall where the wall-pressure intensity $p_{w,\mathrm{rms}}$ equals the static-pressure intensity $p_{s,\mathrm{rms}}$ in the boundary layer. See also Figure 7. Data obtained from DNSs by ●: Skote [12], ▲: Spalart [11], ■: Schlatter and Örlü [5], ▼: Jiménez et al. [6].

tunnel, we find $C_1 = 0.1$, $C_2 = -1.4$ ($x = 21$ m), $C_1 = 0.1$, $C_2 = -1.2$ ($x = 13$ m), and $C_1 = 0.1$, $C_2 = -1.1$ ($x = 8$ m). For the Kyushu wind tunnel, we find $C_1 = 0.03$ and $C_2 = -0.7$.

A significant amount of research has been devoted to wall-pressure measurements. The wall-pressure intensities normalized by inner variables show a large scatter. Bull [33] reported that this uncertainty comes from two main sources. The first source is the spatial resolution of the sensor. If the sensor size is large, high-frequency pressure signals are attenuated, so the accurate pressure intensity, which is the integral of wall-pressure frequency spectrum, cannot be obtained. The other source depends on the configurations of pressure sensors. Bull [33] classified them into four groups: (1) a sensor mounted in a cavity behind the surface pinhole, (2) a sensor mounted behind the pinhole but with no cavity, (3) a sensor mounted behind the pinhole with no cavity, but with the pinhole filled with silicone grease to restore a continuous boundary surface, and (4) a sensor mounted flush with the boundary surface with no surface discontinuity. We used a microphone as the sensor configured by type (1). The experimental techniques and the instruments are kept exactly the same during the measurement at the three facilities. Because the results of the measurements are not the same, we tentatively conclude that the large scatters in wall-pressure intensities are not only due to the two reasons given above but also due to the need to consider the artificial background noise and flow boundary conditions, which are other important factors to be considered. From the comparison of wall pressure between the boundary layer and the channel flow [6], the former flow case exhibits larger pressure intensities. This result is due to the difference of upper boundary conditions and due to the fact that the spatially developing flow affects the wall pressure.

For the inner scaling, the wall-pressure rms increases slowly with Reynolds number. The profiles are well approximated by the relation $p^+_{w,\mathrm{rms}} = 0.94 \times \ln(R_\tau)$ as indicated by the solid line (Figure 12). The behavior of $p_{w,rms}$ normalized by outer variables shows the decreasing trend with increasing Reynolds number, but appears to asymptotically approach a constant value for high R_θ. However, by normalizing the pressure with mixed scaling, we obtain an overall small variation in the normalized rms level, but for high R_θ, it tends to increase slightly. These trends are also observed in the results of DNSs. Although the wall-pressure intensity has been studied so far, the correction due to background pressure

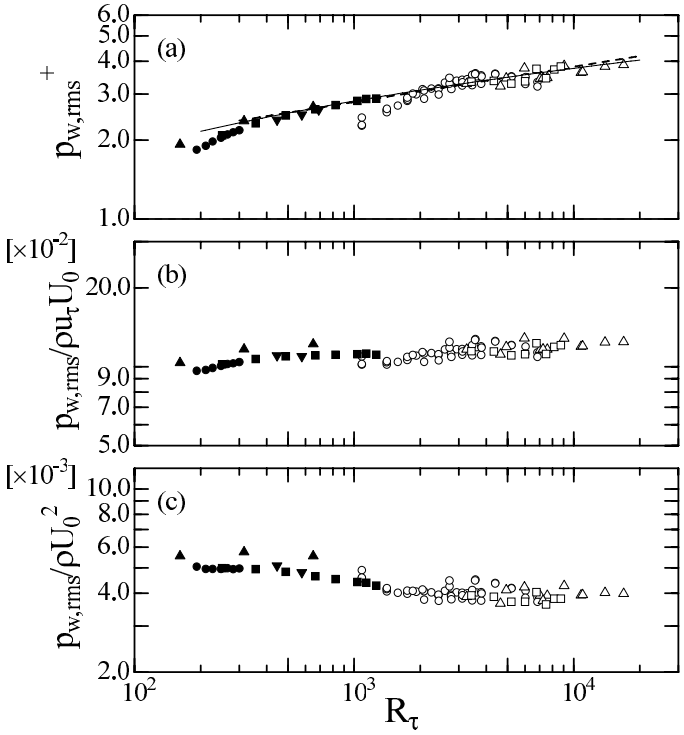

Figure 12. Root mean square of wall pressure normalized by (a) inner scaling, (b) mixed scaling, and (c) outer scaling, as a function of Reynolds number. ◯: pressure measured at the Stockholm wind tunnel, △: pressure measured at the Melbourne wind tunnel, □: pressure measured at the Kyushu wind tunnel. ●: Skote [12], DNS; ▲: Spalart [11], DNS; ■: Schlatter and Örlü [5], DNS; ▼: Jiménez et al. [6], DNS; (dashed line): $(p^+_{\rm rms})^2 = 6.5 + 1.86\ln(R_\tau/333)$ [32]; (solid line): $(p^+_{\rm rms})^2 = 0.94\ln(R_\tau)$.

was not discussed. This correction is small but we think it is necessary for high-fidelity wall-pressure intensity.

4. Conclusions

Using small static-pressure probes, we simultaneously measured the pressure fluctuations, the wall pressure, and the pressure in the free stream in the zero-pressure-gradient boundary layer. We found that the artificial background noise generated inside the wind tunnel influences the physical pressure inside the boundary layer and on the wall pressure. If the background effects are not adequately corrected, the pressure profiles are not similar to the pressure profiles produced by DNS. Flow boundary conditions are other factors that influence the pressure statistics. If we want to know the universality in pressure profiles in the boundary layer, the influence of background noise and flow boundary conditions should be considered.

Acknowledgements

Financial support from the Japan Society for the Promotion of Science (B) 20360083 is gratefully acknowledged. The experiment in Kyushu was supported in part by the Collaborative Research Program of Research Institute for Applied Mechanics, Kyushu University.

We appreciate Prof. Ohya and Mr. Watanabe for their help during the measurements. The support by Dr. R. Örlü, Dr. T. Kurian, and Prof. J. Fransson was indispensable in our measurements. For the Melbourne measurement, we would like to thank Prof. M. Chong for discussions on the shear stress measurements. We would also like to thank our colleagues in the United States, Japan, and Italy for their collaboration.

References

[1] Y. Tsuji, J.H.M. Fransson, P.H. Alfredsson, and A.V. Johansson, *Pressure statistics and their scaling in high-Reynolds-number turbulent boundary layers*, J. Fluid Mech. 585 (2007), pp. 1–40.

[2] Y. Tsuji, J.H.M. Fransson, P.H. Alfredsson, and A.V. Johansson, *Pressure statistics in high-Reynolds number turbulent boundary layer*, in *Proceedings of the Fourth International Symposium on Turbulence and Shear Flow Phenomena*, J.A.C. Humphrey, T.B. Gatski, J.K. Eaton, R. Friedrich, N. Kasagi, and M.A. Leschziner, eds., CD-ROM Publication, Williamsburg, VA, 27–29 June, 2005, pp. 27–32.

[3] Y. Tsuji, *Lagrangian acceleration measurement in fully developed turbulence*, in *Proceedings of the Fifth International Symposium on Turbulence and Shear Flow Phenomena*, R. Friedrich, N.A. Adams, J.K. Eaton, J.A.C. Humphrey, N. Kasagi, and M.A. Leschziner, eds., Technische Universität München, Garching, Germany, August 27–29, 2007, pp. 537–541.

[4] M.S. Monin and A.M. Yaglom, *Statistical Fluid Mechanics*, Vol. 2, The MIT Press, Cambridge, MA, 1971.

[5] P. Schlatter and R. Örlü, *Assessment of direct numerical simulation data of turbulent boundary layers*, J. Fluid Mech. 659 (2010), pp. 116–126.

[6] J. Jiménez, S. Hoyas, M.P. Simens, and Y. Mizuno, *Turbulent boundary layers and channels at moderate Reynolds numbers*, J. Fluid Mech. 657 (2010), pp. 335–360.

[7] J.M. Österlund, *Experimental studies of zero pressure-gradient turbulent boundary layer flow*, TRITA-MEK Tech. Rep. 1999:16, Department of Mechanics, KTH, Stockholm, Sweden, 1999.

[8] T.B. Nickels, I. Marusic, S.M. Hafez, and M.S. Chong, *Evidence of the k^{-1} law in a high-Reynolds-number turbulent boundary layer*, Phys. Rev. Lett. 95 (2005), 074501.

[9] N. Hutchins, T.B. Nickels, I. Marusic, and M.S. Chong, *Hot-wire spatial resolution issues in wall-bounded turbulence*, J. Fluid Mech. 635 (2009), pp. 103–136.

[10] S. Imayama, *High quantitative oil film interferometry and its application to wall bounded flows*, Master's thesis, Department of Engineering and Science, Nagoya University, Japan, 2010.

[11] P.R. Spalart, *Direct simulation of a turbulent boundary layer up to $R_\theta = 1410$*, J. Fluid Mech. 187 (1988), pp. 61–98.

[12] M. Skote, *Studies of turbulent boundary layer flow through direct numerical simulation*, TRITA-MEK Tech. Rep. 2001:01, Department of Mechanics, KTH, Stockholm, Sweden, 2001.

[13] X. Wu and P. Moin, *Direct numerical simulation of turbulence in a nominally-zero-pressure-gradient flatplate boundary layer*, J. Fluid Mech. 630 (2009), pp. 5–41.

[14] K.A. Chauhan, P.A. Monkewitz, and H.M. Nagib, *Criteria for assessing experiments in zero pressure gradient boundary layers*, Fluid Dyn. Res. 41 (2009), 021404.

[15] N.K. Agarwal and R.L. Simpson, *A new technique for obtaining the turbulent pressure spectrum from the surface pressure spectrum*, J. Sound Vib. 135 (1989), pp. 346–350.

[16] G.C. Lauchle and M.A. Daniels, *Wall-pressure fluctuations in turbulent pipe flow*, Phys. Fluids 30 (1987), pp. 3019–3024.

[17] R.L. Simpson, M. Ghodbane, and B.E. McGrath, *Surface pressure fluctuations in a separating turbulent boundary layer*, J. Fluid Mech. 177 (1987), pp. 167–186.

[18] B.E. McGrath and R.L. Simpson, *Some features of surface pressure fluctuations in turbulent boundary layers with zero and favorable pressure gradient*, Rep. No. NASA-CR-4051, NASA Center for AeroSpace Information, Hanover, MD, 1987.

[19] A.M. Naguib, S.P. Gravante, and C.E. Wark, *Extraction of turbulent wall-pressure time-series using an optical filtering scheme*, Exp. Fluids 22 (1996), pp. 14–22.

[20] M.P. Simens, J. Jiménez, S. Hoyas, and Y. Mizuno, *A high-resolution code for turbulent boundary layers*, J. Comput. Phys. 228 (2009), pp. 4218–4231.

[21] T.S. Lund, X. Wu, and K.D. Squires, *Generation of turbulent inflow data for spatially-developing boundary layer simulations*, J. Comput. Phys. 140 (1998), pp. 233–258.

[22] J.H. Lee and H.J. Sung, *Direct numerical simulation of a turbulent boundary layer up to* $R_\theta = 2500$, Int. J. Heat Fluid Flow 32 (2011), pp. 1–10.
[23] A. Ferrante and S.E. Elghobashi, *A robust method for generating inflow conditions for direct numerical simulations of spatially-developing turbulent boundary layers*, J. Comput. Phys. 198 (2004), pp. 327–387.
[24] P. Schlatter, Q. Li, G. Brethouwer, A.V. Johansson, and D.S. Henningson, *Simulations of spatially evolving turbulent boundary layers up to* $R_\theta = 4300$, Int. J. Heat Fluid Flow 31 (2010), pp. 251–261.
[25] K. Liu and R.H. Pletcher, *Inflow conditions for the large eddy simulation on turbulent boundary layers: A dynamic recycling process*, J. Comput. Phys. 219 (2006), pp. 1–6.
[26] M.M. Rai and P. Moin, *Direct numerical simulation of transition and turbulence in a spatially evolving turbulence*, J. Comput. Phys. 109 (1993), pp. 169–192.
[27] J.U. Schlüter, H. Pitsch, and P. Moin, *On boundary layer conditions for LES in coupled simulations*, AIAA Paper 0069, American Institute of Aeronautics and Astronautics, Reston, VA, 2003.
[28] A. Keating, U. Piomelli, E. Balaras, and H.-J. Kaltenbach, *A priori and a posteriori tests of inflow conditions for large-eddy simulation*, Phys. Fluids 16(12) (2004), pp. 4696–4712.
[29] N. Nikitin, *Spatial periodicity of spatially evolving turbulent flow caused by inflow boundary condition*, Phys. Fluids 19 (2007), 091703.
[30] P. Schlatter and R. Örlü, *Turbulent boundary layers at moderate Reynolds numbers: Inflow length and tripping effects*, J. Fluid Mech. (in press), DOI: http://dx.doi.org/10.1017/jfm.2012.324.
[31] P.H. Alfredsson and R. Örlü, *The diagnostic plot – A litmus test for wall bounded turbulence data*, Eur. J. Mech. B/Fluids 29 (2010), pp. 403–406.
[32] T.M. Farabee and M.J. Casarella, *Spectral features of wall pressure fluctuations beneath turbulent boundary layers*, Phys. Fluids 3 (1991), pp. 2410–2420.
[33] M.K. Bull, *Wall-pressure fluctuations beneath turbulent boundary layers: Some reflections on forty years of research*, J. Sound Vib. 190 (1996), pp. 299–315.